Recent atomic clock comparisons at NIST

L. Lorini[1,2,a], N. Ashby[1], A. Brusch[1], S. Diddams[1], R. Drullinger[1], E. Eason[1], T. Fortier[1],
P. Hastings[1], T. Heavner[1], D. Hume[1], W. Itano[1], S. Jefferts[1], N. Newbury[1], T. Parker[1],
T. Rosenband[1], J. Stalnaker[1,3], W. Swann[1], D. Wineland[1], and J. Bergquist[1]

[1] Time and Frequency Division, National Institute of Standards and Technology, Boulder,
   CO 80305, USA
[2] Istituto Nazionale di Ricerca Metrologica INRiM, Strada delle Cacce 91,
   10135 Torino, Italy
[3] Department of Physics and Astronomy, Oberlin College, Oberlin, OH 44074, USA

Abstract. The record of atomic clock frequency comparisons at NIST over the
past half-decade provides one of the tightest constraints of any present-day
temporal variations of the fundamental constants. Notably, the 6-year record of
increasingly precise measurements of the absolute frequency of the Hg^+ single-ion
optical clock (using the cesium primary frequency standard NIST-F1) constrains
the temporal variation of the fine structure constant α to less than $2 \cdot 10^{-16}\,\mathrm{yr}^{-1}$
and offers a Local Position Invariance test in the framework of General Relativity.
The most recent measurement of the frequency ratio of the Al^+ and Hg^+ optical
clocks is reported with a fractional frequency uncertainty of $\pm 5.2 \cdot 10^{-17}$. The
record of such measurements over the last year sensitively tests for a temporal
variation of α and constrains $\dot{\alpha}/\alpha = (-1.6 \pm 2.3) \cdot 10^{-17}\mathrm{yr}^{-1}$, consistent with zero.

1 Introduction

Recently, renewed interest in possible temporal and spacial variations of the fundamental
"constants" was initiated by analyses and modeling of astrophysical and geophysical data that
produced conflicting reports of evidence for their change. Even a small change of a fundamental
constant, either in space or time, would violate one or more tenets of several, widely accepted
physical theories. Further interest has been generated by those theoretical physicists who con-
tinue to work toward a single theory to describe all the forces of nature. So far, a variety of
new and often well-developed theories have emerged, including some string and grand unifica-
tion theories that allow for variation of the fundamental constants in different fashions. The
conflicting evidence of change, and its important ramifications if true, has triggered a number
of experimental efforts toward finding unambiguous evidence of such a variation [1,2].

Much of the experimental work so far has been focused on a search for a variation of the
fine structure constant α. The astrophysical and geophysical studies mentioned above attain
exquisite sensitivity to small temporal changes in α, for example, by looking far back in time, to
physics phenomena that happened long ago. The prominent examples include the 10^9 year old
geochemical remains of the Oklo natural nuclear reactor [3] and the astronomical observations of
spectroscopic absorption lines from distant cosmic clouds using a quasar as the light source [4].
However, the analysis of data from Oklo, as well as that from distant quasars, has suffered from
difficult quantitative interpretations that have produced discrepancies ([5] and [6] for example).

A different approach is to measure the frequency ratios of two or more laboratory atomic
clocks over time. Remarkably, the optical clock ratio measurements have now reached an

---

[a] e-mail: `l.lorini@inrim.it`

accuracy sufficiently high that a yearlong search for a time variation of α, or other fundamental constants, can be done with a sensitivity comparable to, and possibly higher than, that offered by the geological and cosmological observations. High accuracy frequency comparison experiments between atomic clocks are also useful to search for violations of Local Position Invariance (LPI). LPI, which is a fundamental assumption of the Einstein General Relativity, can be tested by looking for correlations between the frequency ratio of two atomic clocks and the change of the gravitational potential due, for example, to the revolution of the Earth around the Sun.

The National Institute of Standard and Technologies (NIST) in Boulder, Colorado (USA), hosts several operational and prototype atomic clocks, including optical atomic clocks based on ^{199}Hg$^+$ [7], ^{27}Al$^+$ [8], Ca [9], Yb [10] and Sr [11] (the Sr optical atomic clock is located at JILA, a joint institute of the University of Colorado and NIST), as well as the Cs primary frequency standard, NIST-F1 [12] and several commercial Hydrogen Masers. This paper reports recent frequency comparison experiments at NIST involving the Hg$^+$ optical atomic clock and NIST-F1, and first results of a direct measurement of the frequency ratio between the Hg$^+$ and Al$^+$ optical clocks. After a comprehensive description of the Hg$^+$ single ion optical frequency standard, which will focus on some technical improvements that were recently introduced, brief descriptions of the Al$^+$ and Cs primary frequency standards will be provided and the techniques for frequency comparison measurements will be briefly discussed. Next, the results of the frequency comparison experiments between Cs and Hg$^+$ and the more recent frequency ratio measurements between Hg$^+$ and Al$^+$ will be explained, focusing on the latest achievements. From the results of these frequency comparison experiments, an estimate of the temporal stability of the constant α will be provided, together with a LPI violation test.

2 ^{199}Hg$^+$ frequency standard

Efforts at NIST to develop and operate an optical clock based on the $5d^{10}6s\ ^2S_{1/2}(F = 0, m_F = 0) \rightarrow 5d^9 6s^2\ ^2D_{5/2}(F = 2, m_F = 0)$ electric-quadrupole-allowed transition ($\lambda \approx 282$ nm) of ^{199}Hg$^+$ have a long history. First proposed as a candidate for an optical frequency standard in the '70s [13], spectral studies of the $S-D$ "clock" transition began with two-photon spectroscopy of a small cloud of buffer-gas-cooled, trapped ^{198}Hg$^+$ in the mid '80s [14]. State detection with nearly unit efficiency of the weakly allowed clock transition by the quantum jump technique [15,16] ushered in high-resolution spectral studies in the Lamb-Dicke regime of single, trapped and laser-cooled ions in the late '80s and early '90s. The development of a sub-Hz, cavity stabilized laser [17,18] provided the means to probe the narrow $S-D$ transition with a resolution limited only by the lifetime (86 ms) of the metastable $^2D_{5/2}$ state. The development of a reliable technique for optical frequency measurements based on femtosecond laser frequency combs (FLFCs) [19,20] provided the first direct measurements of the frequency ratio between the ^{199}Hg$^+$ clock transition and the NIST Cs primary frequency standard (NIST-F1) [21].

2.1 The ion trap

The single Hg$^+$ ion is confined in a spherical Paul trap that is kept in a cryogenic environment at or near the liquid helium temperature of 4.2 K. The cryogenic temperature provides an ultra high vacuum environment where the collisions with background gases are rare and ion lifetimes of several months have been demonstrated [22]. The trap chamber is attached to the bottom of the cryostat and houses the trap, the mercury oven, an ionizing filament, a heater and a fast ($f/1$) imaging lens (figure 1).

Five windows permit optical access to the trap: two opposing ports admit radiation directly to the ion, and two ports offer indirect access to the ion via two relay mirrors that direct the radiation through the center of the trap. The fifth port passes the fluorescence collected by the lens. The trap itself comprises one ring electrode placed between two endcaps (see figure 1). The ring electrode is driven with an oscillating electric field, which is coupled through a helical
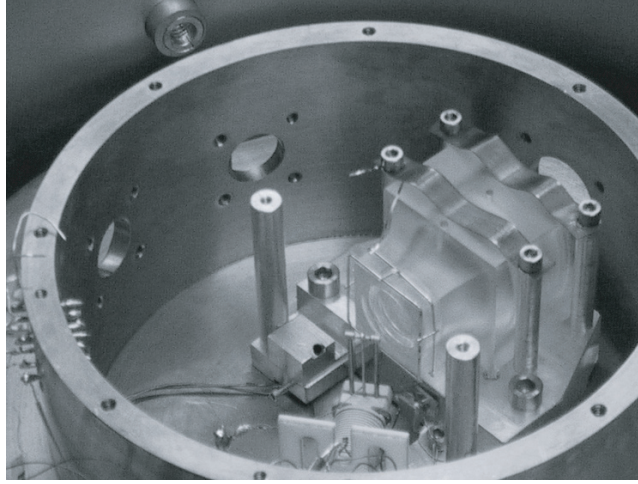
Fig. 1. Photograph of the vacuum chamber that is attached to the bottom of the liquid He dewar. Prominently displayed are the Hg$^+$ ion trap and the fast imaging lens.

coil immersed in the liquid helium bath. The coil tunes out the trap capacitance at approximately 12 MHz. At the usual RF operational parameters, the secular frequencies in the radial plane are nearly degenerate with $\omega_x \approx \omega_y \approx (2\pi \cdot 1250\,\mathrm{kHz})$ and the secular frequency along the trap axis $\omega_z \approx (2\pi \cdot 2300\,\mathrm{kHz})$ is about twice that of the radial frequencies. The two endcaps are AC grounded, but DC voltages can be applied to the endcaps as well as to two other compensation electrodes, which are positioned 90 degrees apart and perpendicular to the trap axis, to balance the effect of any stray charges. In this way the ion can be centered at the nodal position of the applied oscillating RF electric field to minimize the second order Doppler shift and AC Stark shift associated with micromotion at the RF drive frequency.

2.2 Laser cooling and state preparation

The $5d^{10}6s\ ^2S_{1/2} \rightarrow 5d^{10}6p\ ^2P_{1/2}$ first resonance line of ^{199}Hg$^+$, dressed by its hyperfine structure, is used for laser cooling, clock-state preparation and clock-state detection (see figure 2(a) for a simplified optical level diagram of the relevant components). The natural linewidth (FWHM) of each component is about 55 MHz.

The cycling transition $^2S_{1/2}, F = 1 \rightarrow\ ^2P_{1/2}, F' = 0$ at 194 nm is used for all three tasks, cooling, state-preparation, and state-detection. About 150 μW of single frequency radiation at 194 nm is synthesized by mixing light at 257 nm with light at 792 nm in an angled-tuned BBO crystal. More than 500 mW of single frequency power at 792 nm is derived from a titanium sapphire (Ti:S) laser and amplified 100-fold by means of a power enhancement cavity placed around the BBO crystal, while about 150 mW of light power at 257 nm beam is singly passed through the crystal collinear with the 792 nm radiation [23]. The 257 nm light is harmonically generated in a second BBO crystal from light at 515 nm produced by a single-frequency Ar$^+$ ion laser [23]. The Ar$^+$ ion laser is prestabilized by locking its frequency to a low-finesse cavity, which in turn is locked to a saturated absorption feature of molecular iodine. A second Fabry-Perot cavity, with mirrors coated for both 515 and 792 nm, is then locked to the frequency of the stabilized Ar$^+$ ion laser. The sum frequency generated 194 nm radiation can then be precisely tuned or fixed with respect to the mercury ion resonance by locking the frequency of the 792 nm radiation to a fringe of the stabilized cavity with either a tunable or fixed offset with respect to the frequency of the Ar$^+$ laser. The $^2S_{1/2}, F = 1 \rightarrow\ ^2P_{1/2}, F' = 0$ is a cycling transition only as a first approximation, When the ion is held in a zero-field environment and irradiated by light that is tuned near the cycling transition frequency C (see figure 2(a)), it is pumped rapidly into a non-interacting state. Even in a non-zero but low magnetic field environment (magnetic
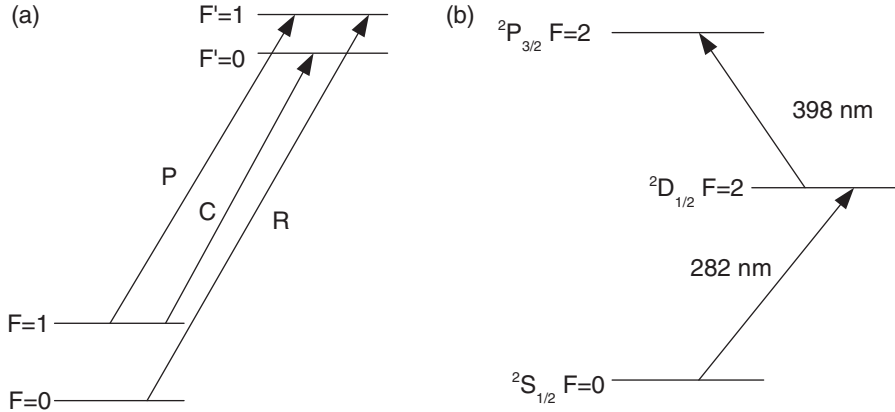
Fig. 2. (a) A simplified optical level diagram showing hyperfine structure (not to scale) of the $^2S_{1/2} \to \, ^2P_{1/2}$ transition in ^{199}Hg$^+$. Also indicated are the cycling transition C, the repumping transition R, and the pumping transition P. See text for details. (b) Hg$^+$ clock transition and auxiliary transition used to quickly empty the metastable state.

substates not resolved), such as that used in the normal operation of the Hg$^+$ optical clock, the ion is quickly pumped into a non-interacting superposition of the magnetic sublevels of the $^2S_{1/2}$ $(F = 1)$ state [24]. In the present configuration of the experiment, these "dark" states are eliminateded by irradiating the ion with three non-collinear beams at different frequencies. The beams are generated by passing the 194 nm radiation through an acousto-optic modulator (AOM) driven by three, equally spaced RF signals at 104, 120 and 136 MHz. The central component is red detuned from the $^2S_{1/2}, F = 1 \to \, ^2P_{1/2}, F' = 0$ cycling transition by nearly a half linewidth ($\approx$28 MHz), and is steered directly onto the ion through one of the window ports. Two meters from the AOM, the two sideband beams are spatially resolved and directed separately onto the ion through two other window ports and independent mirror relay systems. The three non-collinear beams are made to intersect at the site of the ion, where the light-field polarization continually changes because of the beams' disparate frequencies, thereby preventing dark states [25]. However, even with the elimination of these dark states, off resonance scattering through the $^2P_{1/2}, (F' = 1)$ level removes the ion to the $^2S_{1/2}, (F = 0)$ state, 40.5 GHz off resonance with the cycling transition C. Since this occurs with a small probability ($\approx 10^{-4}$), a lower power beam tuned to match the frequency of the $F = 0 \to F' = 1$ line (R in figure 2(a)) easily returns the ion to the $F = 1$ state and the fluorescence from the cycling transition C is restored. Prior to probing the clock transition, the ion is prepared in the $^2S_{1/2}, (F = 0)$ state by means of a third laser beam tuned to resonance with the $F = 1 \to F' = 1$ component (P in figure 2(a)), which quickly "pumps" the ion into the $F = 0$ state. This recently introduced laser has reduced the time required for the state preparation from about 15 ms to 1–2 ms [26]. The R and P light is generated by sum-frequency-mixing the 792 nm radiation from two extended cavity Hg$^+$ diode lasers (ECDL) in Littman configuration with the same radiation source at 257 nm as is used for generating radiation source C. The radiation from the two independently tunable diode lasers is superimposed with the Ti:S beam in the power enhancement cavity where the 194 nm light C is produced. One mode of the cavity is servoed to resonance with the frequency of the Ti:S laser using the Haensch-Couillaud technique [27], while the frequencies of the two diode lasers are each kept in resonance to their own cavity mode by means of a phase-lock to the frequency of the Ti:S laser (see figure 3).

The FHWM of each spectral component of the $^2S_{1/2} \to \, ^2P_{1/2}$ transition is about 55 MHz, or about 1/3 the free spectral range ($\approx$162 MHz) of the enhancement cavity. Hence, when all three lasers are made simultaneously resonant with their respective cavity modes, the cavity length can be adjusted to bring both diode lasers into resonance, or nearly so, with their corresponding spectral component of the $^2S_{1/2} \to \, ^2P_{1/2}$ transition. In the worst case, the R or P radiation is never more than about a linewidth away from its respective line resonance. Even in this case,
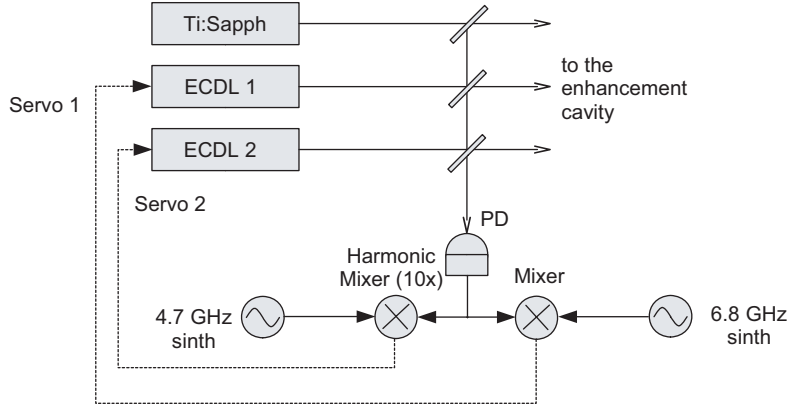
Fig. 3. ECDL frequency lock circuit. The light from the Ti:S and the two ECDLs is sent to an ultrafast photodiode (PD) and two beatnotes are extracted and referenced to the two synthesizers with two PLLs. The servo acts both on the diode current (fast, short range) and cavity (slow, long range).

the power from either diode lasers is adequate for effective repumping or pumping to ground state.

2.3 Clock radiation synthesis and stabilization

Previously, the clock radiation was synthesized by Second Harmonic Generation (SHG) of a dye laser operating at 563 nm. In the latest version, schematically shown figure 4, the dye laser has been replaced by a frequency doubled Yb-doped fiber laser, operating at 1126 nm. The power of this "master" laser is boosted to about 600–700 mW with an Yb-doped fiber amplifier and then doubled to 563 nm using a non-critically phase-matched LBO crystal placed in the tight waist of a power enhancement cavity.

The cavity is a 4-mirror ring, with a FSR of ≈575 MHz and a power enhancement of about 100. The transmission coefficient of the input coupler is about 0.7%, which gives a near optimal impedance match for 550 mW in and 175 mW of green power out. The cavity is servoed to resonance with the laser using the Haensch-Couillaud technique [27]. The prestabilization cavity that was used to narrow the free running linewidth of the dye laser is not needed in the new setup. Instead, the harmonic green light at 563 nm generated in the SHG stage is sent directly through an optical fiber to an acoustically isolated room which hosts the high-finesse cavity to which the laser is referenced using the Pound-Drever-Hall technique [28]. The spectral character and frequency stability of the dye laser locked to performance of the high-finesse cavity, which is supported on an isolation platform suspended by latex tubing, and of laser lock have been described in detail elsewhere [18]. Because the spectral properties and feedback control elements of the fiber laser differ from those of the dye laser, a few details of the laser lock have been changed. The frequency of the laser is slaved to a resonance of the high-finesse cavity using three different stages driving distinctly separate control elements, each with a different bandwidth and dynamical range. The slowest stage possesses the largest dynamical range and acts on a piezo that stretches the laser fiber. The feedback of the intermediate stage acts on an AOM that is placed at the infrared output of the master laser and prior to the fiber amplifier. Its dynamical range is limited to a few MHz since the AOM is single passed and coupled to a single mode fiber. The correction signal of the fastest stage, which is AC coupled only, acts on an AOM that intercepts the green 563 nm light beam from the doubling cavity prior to the high-finesse cavity. The green light, well stabilized to the cavity [18], is sent through yet another AOM and optical fiber from the isolation platform to the ion table. This AOM acts both as a servo for the fiber noise cancellation and to steer the laser frequency away from the cavity resonance and onto resonance with the Hg$^+$ clock transition. The 563 nm radiation is single-passed through a final AOM that is used to step the frequency of the laser back and forth
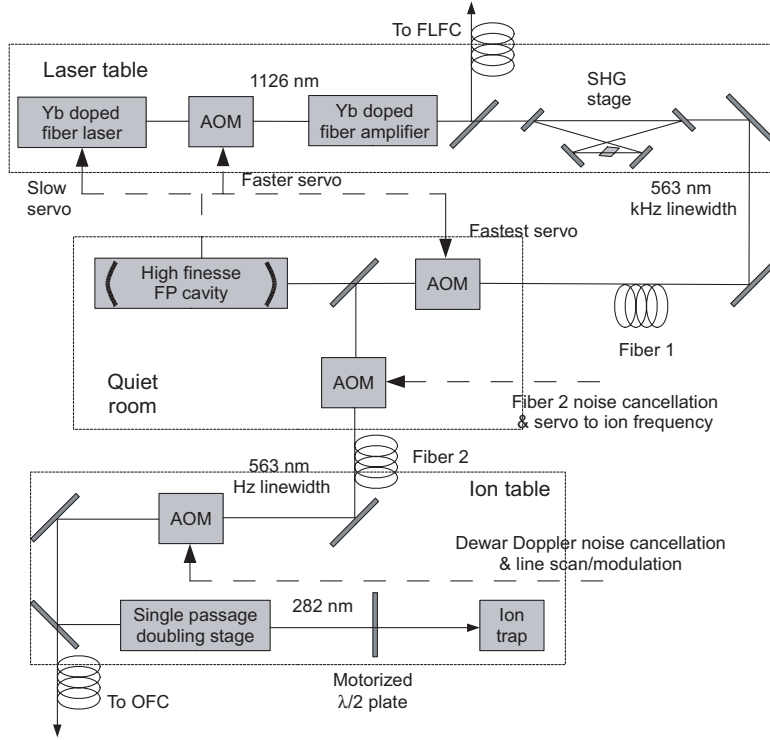
Fig. 4. Synthesis and stabilization of the Hg$^+$ clock radiation.

across the ion resonance (stepping AOM). The modulated light exiting this AOM is doubled to 282 nm in a non-critically phase-matched deuterated AD*P crystal and steered onto the ion. The stepping AOM also serves to cancel the Doppler noise associated with motion of the trap, caused, for example, by the always boiling cryogens.

2.4 Interrogation and readout

After the ion has been prepared in the state $^2S_{1/2}(F = 0)$, as described in section 2.2, the clock transition is driven by a single (Rabi) pulse with a typical probe time of 40–60 ms. Subsequently to the Rabi pulse, C and R components (figure 2) are simultaneously turned on for a 5–10 ms detection period. If the clock transition did not occur, then the ion remains in the $^2S_{1/2}(F = 0)$ state and 194 nm fluorescence is observed and counted (typically, 12–15/ms). If the clock transition did occur, then the ion is in the $^2D_{5/2}(F = 2)$ state and no fluorescence is observed (typically, less than 1/s background scattered light) [15]. If the ion is allowed to remain in the metastable $^2D_{5/2}$ state until it naturally relaxes ($t_D \approx 86$ ms), then the efficiency of the clock cycle is reduced by this "dead" time and the stability is degraded. In the latest version of the Hg$^+$ clock, the $^2D_{5/2}$ state is quickly emptied (in less than 1 ms) following each detection period by irradiating the ion with radiation from a blue ECDL tuned to resonance with the $^2D_{5/2}(F = 2) \rightarrow {}^2P_{3/2}(F = 2)$ transition at 398 nm. The $^2P_{3/2}(F = 2)$ state relaxes in a few ns with high probability to the ground state [29]. Hence, the dead time is importantly reduced and the clock stability improved.

The Hg$^+$ clock operations are automatically driven by software and the clock cycle is looped continuously; the probability for the clock transition is calculated modulating the probe laser across the atomic resonance frequency and the gathered information is then used to steer the laser frequency. The algorithm for the laser frequency servo, completely assisted by computer, uses dedicated algorithms to correct for signal amplitude fluctuation and cavity frequency drift [26]. The introduction of the two laser radiations for pumping to $^2S_{1/2}(F = 0)$ (described

in section 2.2) and to empty the metastable state has reduced the cycle dead time from about 80 ms to about 20 ms, improving the clock duty cycle from 33% to 66% [26].

2.5 Accuracy of the Hg$^+$ standard

The various contributions to the systematic fractional frequency uncertainty of the Hg$^+$ optical clock have been described in detail previously [30]. Since then, the uncertainty due to some contributions have been constrained to a lower value. A summary of the contributions to the total systematic fractional frequency uncertainty σ, which is now evaluated to be $\sigma < 1.9 \cdot 10^{-17}$, is reported in detail in Table 1, together with the fractional frequency shift $\Delta\nu/\nu$:

Table 1. Leading contributions to the systematic uncertainty budget of the Hg$^+$ optical clock ($\times 10^{-18}$).

Shift	$\Delta\nu/\nu$	σ	Limitation
2nd order Doppler − Micromotion	−4	4	Static electric field
2nd order Doppler − Secular motion	−3	3	Doppler cooling
DC quadratic Zeeman	−1130	5	Calibration with 1st order sensitive line
AC quadratic Zeeman	0	10	Current leakage from trap electrodes
Quadrupole shift	0	10	B-field orientation
1st order Doppler − Synchronized motion	0	7	Probe beam alignement
Background gas	0	4	Collisions rate (with He)
AOM phase chirp	0	6	AM to PM conversion for the AOM
Total	−1137	19	

The residual motion of the laser-cooled ion gives rise to a fractional frequency uncertainty associated with the relativistic Doppler shift. The uncertainty due to the secular motion is constrained to $4 \cdot 10^{-18}$ when the ion is cooled to near the Doppler cooling limit; the uncertainty due to residual micromotion is also constrained to $4 \cdot 10^{-18}$ when the trap is well balanced. The micromotion of the trap is continuously monitored [31], and, if need be, corrected using small bias voltages applied to either endcap and/or to two bias electrodes that lie exterior to the trap, are orthogonal to its axis and lie 90° apart. The maximum AC Zeeman shift due to any asymmetry of the RF currents flowing in the trap electrodes was estimated to be less than $1.0 \cdot 10^{-17}$. We believe this latest estimate to be conservative because it postulates an imbalance of 25% in the RF currents flowing in the trap electrodes [32]. The clock transition is first-order field insensitive at zero field, whereas the second-order sensitivity is approximately $-(188\,\mu\text{Hz}) \cdot B^2$ (B in μT). The quadratic field shift of the clock transition due to the small ($8\,\mu$T) applied quantization field is effectively monitored during the measurement run by occasionally interleaving a frequency measurement of the first-order field sensitive $^2S_{1/2}(F = 0, m_F = 2) \to\, ^2D_{5/2}(F = 2, m_F = 2)$ component with the regular clock cycles. Slow variations of the magnetic field presently limit the uncertainty of the DC quadratic Zeeman shift to $5 \cdot 10^{-18}$.

The electronic charge density of the $^2D_{5/2}$ state has an electric quadrupole moment that can produce an energy shift in the presence of a static electric field gradient. The magnitude and sign of the shift depend on the relative orientation of the field gradient and the applied field, which offers a route to its cancellation [33]. Typically, the fractional frequency shift is less than 10^{-16}, but due to our inability to know, much less control the ambient field gradient, the uncertainty is equally as large as 10^{-16} [7]. However, the quadrupole shift, as well its uncertainty, can be effectively eliminated by averaging the clock frequency for three mutually perpendicular field quantization axes [33]. In our realization of this scheme, the orientation of the three axes and the probe light polarization were chosen to give the same scattering rate for the clock transition over the three directions of the applied field [30]. Changing the field direction at regular intervals (typically, every 300 s) and steering the frequency of the clock

laser to resonance with the ion at each field setting are completely automated. The average clock frequency for the three field directions is without the quadrupole shift with a residual uncertainty estimated smaller than 10^{-17}, that is due to the slight non-orthogonality of the three applied fields.

Another potential shift arises from the pulsed interrogation and detection sequence. If the ion is caused to move synchronously with each clock cycle, this would cause a first-order Doppler shift with a nonzero average. This synchronized movement could have different sources, for example, the creation of photoionization charges on the trap electrodes due to the scattering of UV light. The systematic shift from this effect is potentially large, as a synchronized velocity of only 10^{-8} m/s due to few photoionization charges, would cause a Doppler shift of $3 \cdot 10^{-17}$ [32]. The effect can be measured and averaged down by alternately probing the ion clock resonance with collinear but counter-propagating beams; no shift was detected at the $7 \cdot 10^{-18}$ level. This value is limited by the unequal statistical weight of probe directions and can be greatly reduced by averaging equally during the measurement run.

The cryogenic surfaces cryo-pump all gases with the possible exception of He (which is also cryo-pumped until a monolayer is established). Possible sources of He are leaks in the indium seals as well as through the Dewar windows that are permeable to He. An upper limit to the He partial pressure was set at $7 \cdot 10^{-10}$ Pa using a quadrupole mass analyzer, which is conservatively estimated to give a maximum fractional frequency shift of $4 \cdot 10^{-18}$ [32]. An often ignored frequency shift is caused by the thermal loading of any AOM in the clock beam path that is turned on and off, such as the stepping AOM used here to probe either side of the clock resonance. The shift scales linearly with RF power, but diminishes with the ratio of time-on to time-off. The typical level of applied power during the probe "on" phase gives a maximum fractional frequency shift of $6 \cdot 10^{-18}$.

3 ^{27}Al$^+$ frequency standard

Several years ago, Dehmelt first noted some of the pertinent features of the group IIIA ions that made them attractive candidates for optical clocks of unprecedented stability and accuracy [15]. In particular, the weakly allowed $^1S_0 \rightarrow {}^3P_0$ intercombination line at 267 nm in ^{27}Al$^+$ seems to offer most, if not all, of the essential ingredients for building a single-ion optical clock with exceptional stability and accuracy, for example:

- The 20 s lifetime of the metastable $^3P_0$ state gives rise to a natural line Q that exceeds 10^{-17} [8].
- The electronic charge density of the $J = 0$ states does not support an electric quadrupole moment and, absent a quadrupole moment, there is no electric quadrupole shift.
- The blackbody radiation shift is very small; the fractional shift is about $-1 \cdot 10^{-17}$ at 50 °C.

But, unfortunately, the wavelength of the strongly allowed first resonance transition in ^{27}Al$^+$ is at 167 nm, an impractical color for laser cooling and detection. To overcome this limitation, the Al$^+$ ion is trapped in a linear Paul trap together with a ^{9}Be$^+$ ion, which has a cycling transition at a convenient wavelength for laser cooling. In this configuration, the motional degrees of freedom of both ions are coupled via the coulomb interaction making it possible to sympathetically cool the Al$^+$ ion down to the Doppler limit by laser-cooling the Be$^+$ ion [34]. Furthermore, the superposition state of the clock ion can be faithfully transferred to the Be$^+$ ion through one of their shared motional states using some of the techniques of quantum information processing. This makes it possible to determine the clock state of the Al$^+$ ion (or of any clock ion) by the presence or absence of fluorescence from the Be$^+$ ion [35]. For completeness, we briefly summarize the latest version of the Al$^+$ ion clock here; the realization of the Al$^+$ optical clock using quantum logic spectroscopy is discussed in greater detail elsewhere [8,36]. Subsequent to its coherent interaction with the driving field radiation of the clock laser, the Al$^+$ ion is in a coherent superposition of the $^1S_0$ and $^3P_0$ states. This superposition can be (and has been) mapped directly onto the Be$^+$ ion through a shared motional mode, but the

fidelity of the measurement of the projected clock state suffers from the relatively small number (6–9) of scattered photons detected before the Be^+ knowledge of the projected clock state is "destroyed". However, the projected clock state information still remains intact with the Al^+ clock and can be repetitively retrieved and sent to the Be^+ ion to be re-read. As a technicality, the original Al^+ clock state is projected out with a Raman pulse applied to the $^1S_0 \rightarrow ^3P_1$, which simultaneously entangles the $^1S_0$, $^3P_1$ states and (typically) the center-of-mass motional degree of freedom. It is the only time that quantum logic is actually used in any one clock cycle; in the repetitive QND probes and readouts of the projected clock state, no further entanglement is made. An adaptive algorithm is used to optimize the number of repetitive read-outs made. Typically, 4–5 iterations are made and a fidelity of 99.94% is reached for the Al^+ clock state detection [37]. Since every transition between magnetic sublevels of the Al^+ clock states suffers a first-order linear field shift, which can be as high as few kHz at the operational magnetic field, the stretched magnetic substate's are alternately probed to zero the first-order Zeeman shift. The fractional frequency uncertainty of the standard was evaluated as $2.3 \cdot 10^{-17}$ [32]. The main contribution to the uncertainty is due to the second-order Doppler shift caused by the residual ion movement related to the secular motion and to the micromotion. Other minor contributions are due to the Zeeman quadratic shift and to the AC Stark shift caused by blackbody radiation at room temperature, which is fractionally of order 10^{-16} and has been measured in [38].

4 The Cs fountain primary frequency standard

The NIST-F1 cesium primary frequency standard was widely described in [12], and more recent updates were reported in [39]. When the NIST-F1 is running, its frequency is compared with the frequency of an hydrogen maser (H-maser), which acts as a transfer oscillator for local and remote frequency comparison [40]. The fractional systematic frequency uncertainty for the most recent measurements reported in this paper is about $4.1 \cdot 10^{-16}$; the largest contributions to the uncertainty comes from the evaluation of DC Zeeman shift due to the quantization magnetic field, by the spin exchange collisions between cold Cs atoms and the AC Stark shift due to the blackbody radiation at room temperature. The operational density of cold Cs atoms is chosen to trade off between statistic and spin exchange collision uncertainty. During the most recent frequency comparison experiments with Hg^+, NIST-F1 was operated with a statistic fractional frequency uncertainty of $2 \cdot 10^{-13} \, \tau^{-1/2}$.

5 Optical frequency measurements

5.1 Optical frequency measurements techniques using Femtosecond Laser Frequency Combs

Both the Al^+ and the Hg^+ clock lasers are connected with optical fiber links to an octave spanning Ti:Sapphire Femtosecond Laser Frequency Comb (FLFC) [41] and to an Er:fiber FLFC [42]. Because the clock laser for either standard starts as a stabilized infrared fiber laser, the IR light from each one is sent to both FLFCs. And in both cases, the light frequency measured by the FLFCs differs by a fixed amount with respect to the fourth subharmonic of the atomic resonance frequency. The spectral purity of the ion clock lasers is preserved at the FLFC locations exploiting fiber noise cancelling techniques [43].

The octave spanning Ti:Sapphire FLFC has been described in detail elsewhere [41]. When it is used in the optical clock configuration, one tooth of the comb is phase locked to one of the clock laser and the carrier envelope frequency ν_{ceo} is phase locked to a RF source. When so locked, the comb repetition rate frequency ν_{rep} is given by the following formula:

$$\nu_{rep} = \frac{\nu_{L1} \pm \nu_{b1} \pm \nu_{ceo}}{n} \qquad (1)$$

where ν_b is the beatnote frequency between the clock laser frequency ν_{L1} and a nearby comb tooth, n is the order of the involved tooth and ν_{b1} and ν_{ceo} are fixed by the PLLs. The order
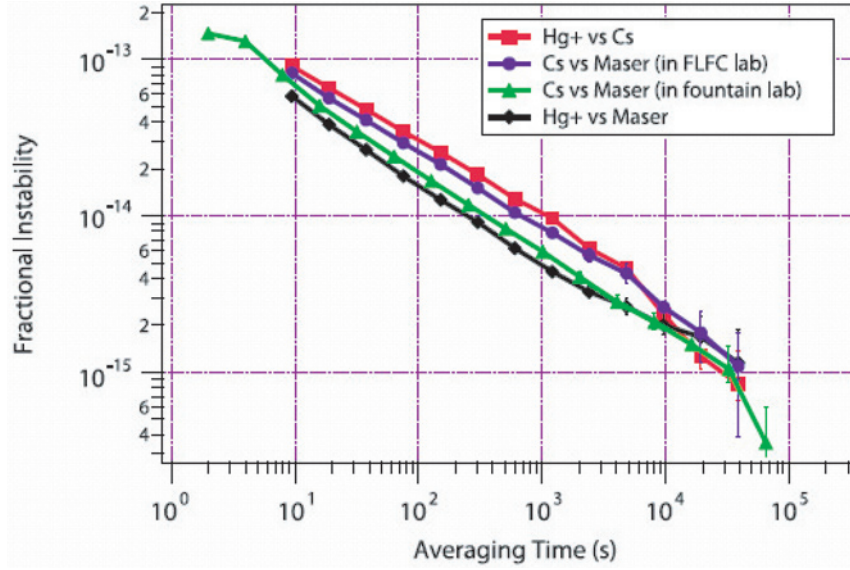
Fig. 5. Stability plot for the most recent Hg$^+$ vs. NIST-F1 measurement run.

n and the correct signs are typically chosen by a coarse determination of ν_{L1}. In the measurements reported here, the FLFCs were locked to either the Hg$^+$ or Al$^+$ clock lasers. When the frequency of the Hg$^+$ clock laser is compared with the NIST-F1 primary frequency standard, ν_{rep} is measured by a frequency counter whose timebase is referenced by the H-maser that serves as the transfer oscillator for NIST-F1. When a measurement of the frequency ratio of the two optical clocks is taken, as in the case of the Al$^+$/Hg$^+$ frequency ratio measurement, the comb is locked to the laser oscillating at the frequency ν_{L1} and the beatnote ν_{b2} between the laser oscillating at the frequency ν_{L2} and the a nearby tooth is counted. The frequency ν_{L2} is given by:

$$\nu_{L2} = n'\nu_{rep} \pm \nu_{ceo} \pm \nu_{b2} \tag{2}$$

where n' is the tooth order which is chosen, as well as the sign, by the coarse knowledge of ν_{L2}. Using the (1) and the (2), ν_{L2}/ν_{L1} is calculated as:

$$\frac{\nu_{L2}}{\nu_{L1}} = \frac{n'\nu_{rep} \pm \nu_{ceo} \pm \nu_{b2}}{n\nu_{rep} \pm \nu_{ceo} \pm \nu_{b1}}. \tag{3}$$

If ν_{b2} and ν_{ceo} are, respectively, measured and locked, with respect to the same RF reference, the uncertainty of this reference does not affect the ν_{L2}/ν_{L1} value.

5.2 Hg$^+$ versus NIST-F1 measurements

During the period between 2000 and 2006, more than 25 measurements of the absolute frequency of the Hg$^+$ optical clock were made. On some occasions, NIST-F1 and the optical clock ran simultaneously, otherwise the absolute frequency was determined using the H-maser as a frequency flywheel. In all measurements since 2005, the two standards were on simultaneously. And during the six year period in which the absolute frequency of the Hg$^+$ optical clock was measured, different versions of the FLFC were used [41,44,45]. In this report, we focus on the most recent measurement, which was made in March 2006. The duration of that measurement run was about about 40 hours, with only a 20% dead time for the Hg$^+$ clock. Figure 5 shows the fractional frequency instability estimated using the Allan Deviation.

The fractional frequency instability is limited by the statistical uncertainty of NIST-F1 at short and medium measurement times and by the H maser at long times. However, since the H
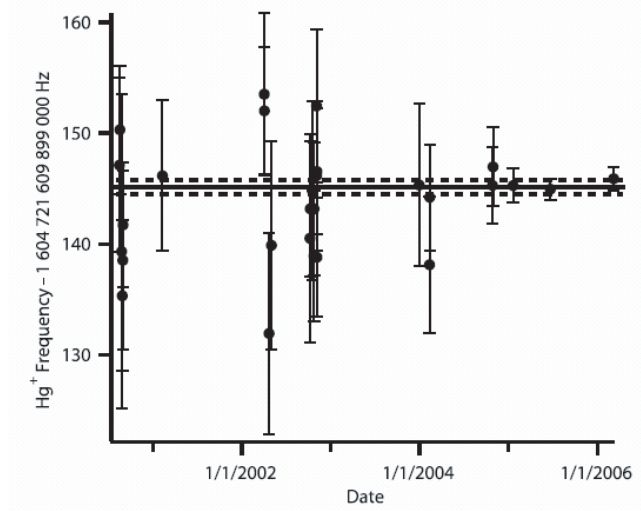
Fig. 6. Historical record of the Hg$^+$ vs. NIST-F1 measurements. The solid line indicates the weighted mean and the dashed lines bound the uncertainty of the mean.

maser is used as a transfer oscillator, its contribution is almost completely removed as NIST-F1 runs with negligible dead time [46]. A fit to the Hg$^+$ vs. NIST-F1 data in figure 5 gives a fractional frequency instability of $3 \cdot 10^{-13} \tau^{-1/2}$. Correcting for systematic offsets, the final value for this measurement run is

$$\nu_{Hg^+} = 1\,064\,721\,609\,899\,145.89(1.06)\,\text{Hz}. \tag{4}$$

The reported uncertainty is dominated by the statistical uncertainty of the measurement and not by the systematic uncertainties of either standard. This value is in agreement with previously published results [47,48]. Figure 6 reports all the measurements performed during the period 2000–2006. Much of the earlier data were assigned a conservative fractional frequency uncertainty of 10^{-14} because of a conservative allowance made for the electric quadrupole shift, which until 2005 had only been estimated. Subsequent to a measurement of the electric quadrupole moment [7], the fractional frequency uncertainties of the earlier data were readjusted to a lower value.

A detailed analysis of all the data reported in figure 6 has been performed elsewhere [49], in which the measurement values and their uncertainties (and any adjusted uncertainties) are discussed in light of the different measurement and data analysis techniques. The weighted mean of all the data is

$$\nu_{Hg^+} = 1\,064\,721\,609\,899\,145.30(69)\,\text{Hz}. \tag{5}$$

5.3 Al$^+$/Hg$^+$ frequency ratio measurements

When measuring the frequency ratio of Al$^+$ to Hg$^+$, the FLFCs record data every second. The duration of a typical run is several hours, and is usually limited by the lifetime of the Al$^+$ ion in the trap. Figure 7(a) shows the fractional frequency instability of the two optical standards for a typical run using two estimators; the two-sample Allan Deviation and the overlapping sample deviation. For integration times longer than $100\,$s, when the frequencies of the optical clocks are fully steered by the atoms, the fractional frequency instability is $3.9 \cdot 10^{-15} \tau^{-1/2}$ [32].

The fractional frequency instability has been decreased by almost a factor of two with respect to the earlier measurements. This improvement is due mainly to improving the duty cycle for the Hg$^+$ optical clock by nearly a factor of two, to a new high finesse cavity for the Al$^+$ clock and to the optimization of the Al$^+$ cooling process that allowed a longer probe time.

Figure 7(b) shows the frequency ratio measurements of Al$^+$ to Hg$^+$ from December 2006 to December 2007. The accuracy evaluation for the optical clocks that include first order Doppler
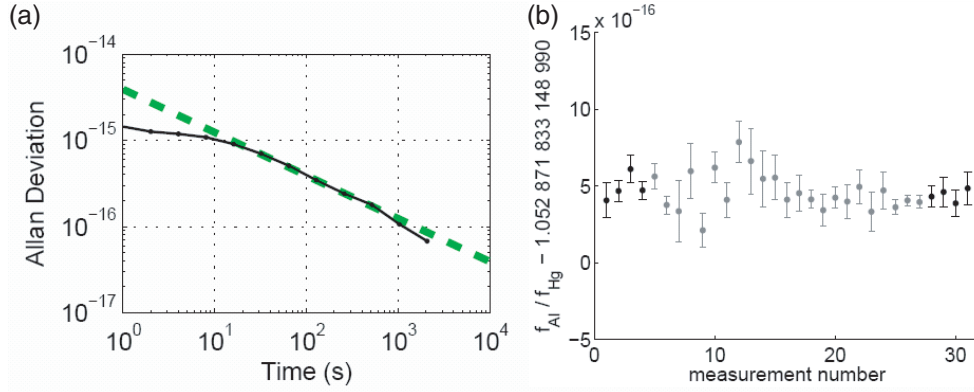
Fig. 7. (a) Stability plot for the most recent Al^+/Hg^+ frequency ratio measurement. (b) Historical record of the Al^+/Hg^+ measurements. Only the last four points have a comprehensive 1st order Doppler shift evaluation.

shifts synchronized with the probe times has been carried out only for the last four points. The weighted average of the frequency ratio from these measurements, is [32]

$$\nu_{Al+}/\nu_{Hg+} = 1.052\,871\,833\,148\,990\,44(5). \tag{6}$$

The systematic fractional frequency uncertainties of Hg^+ $(1.9 \cdot 10^{-17})$ and Al^+ $(2.3 \cdot 10^{-17})$ contribute by nearly the same amount to the overall fractional frequency uncertainty of their ratio $(5.2 \cdot 10^{-17})$. The fractional frequency uncertainty of the ratio is dominated by the statistical fractional frequency uncertainty of the measurement $(4.3 \cdot 10^{-17})$. The statistical dispersion of the earlier data (first 27 points in figure 7(b)) with respect the last four data does not show pathologies, and offers confidence in the reproducibility of the earlier measurements. For the latter data shown in figure 7(b), the Hg^+/Al^+ frequency ratio measurements were made simultaneously by the two FLFCs, the Ti:S and the Er:fiber. The measurements of the two completely independent FLFCs were consistent to the order of the fractional frequency uncertainty of the ratio measurement made by either FLFC [50].

6 Test on physical theories

6.1 Test on the temporal stability of α

The fine structure constant $\alpha = \frac{e^2}{4\pi\epsilon_0\hbar c}$ is the natural scaling factor for the energies involved in atomic spectroscopy. Transition frequencies from electronic (gross), fine (FS) and hyperfine (HFS) structure can be written as a function of a non-relativistic part, which depends only on the structure involved in the transition, and a relativistic part $F_j(\alpha)$, which depends on the specific transition j that is considered. Thus the transition frequencies can be written in the following manner:

$$\begin{aligned} \nu_j(el) &= R_y F_j(\alpha) \\ \nu_j(FS) &= \alpha^2 R_y F_j(\alpha) \\ \nu_j(HFS) &= \alpha^2 \frac{\mu}{\mu_B} R_y F_j(\alpha), \end{aligned} \tag{7}$$

where R_y is the Rydberg constant, $\frac{\mu}{\mu_B}$ is the ratio between the magnetic moment of the nucleus μ and the Bohr magneton μ_B. The theory and the notation used here come from [51–53]. Relative sensitivity of $\nu_j(el)$ and $\nu_j(HFS)$ with respect to a temporal variation of fundamental constants

can be written taking the logarithm and then differentiating with respect to the time the first and the third term of equation (7):

$$\frac{d\ln\nu_j(el)}{dt} = \frac{d\ln R_y}{dt} + N_j\frac{d\ln\alpha}{dt}$$
$$\frac{d\ln\nu_j(HFS)}{dt} = \frac{d\ln R_y}{dt} + \frac{d\ln(\mu/\mu_B)}{dt} + (2+N_j)\frac{d\ln\alpha}{dt},$$

(8)

where N_j in equation (8) is defined as $N_j = \frac{d\ln F_j(\alpha)}{d\ln\alpha}$.

Temporal variation of R_y is common to all transition frequencies and its contribution is removed from frequency ratio measurements. The term N_j contains the dependence of the specific transition involved; it can be either positive or negative, and tends to be larger for transitions involving heavier atoms, where relativistic corrections play a more important role for the atomic energies. Values of N_j have been calculated for several electronic transitions of atomic and molecules of cosmological and laboratory interest, including Hg^+ [4] and Al^+ [54], as well as for HFS transitions in the microwave spectral region involved in high precision spectroscopy and atomic frequency standards [4].

Here we report two tests for α variation using the results coming from the Hg^+ vs. Cs and Hg^+ vs. Al^+ experiments described in the previous sections. The temporal sensitivity of the ratio between Hg^+ and Cs can be written in the following way:

$$\frac{\frac{d}{dt}\left(\frac{\nu_{Hg^+}}{\nu_{Cs}}\right)}{\frac{\nu_{Hg^+}}{\nu_{Cs}}} = \frac{\dot{\alpha}}{\alpha}N - \frac{d}{dt}\ln\left(\frac{\mu_{Cs}}{\mu_B}\right),$$

(9)

where $N = N_{Hg+} - N_{Cs} - 2$ and $N_{Hg+} \approx -3.2$, $N_{Cs} \approx 0.8$.

Both α and $\left(\frac{\mu_{Cs}}{\mu_B}\right)$ can vary with time and, with the help of data coming from frequency comparison experiments between different optical clocks and Cs, which provide different values for N, it is possible to estimate the variation of α and $\left(\frac{\mu_{Cs}}{\mu_B}\right)$ at the same time. This kind of analysis has been performed with a technique described in [55] and the results reported here come from [52]. This analysis uses the following data from frequency comparison experiments between optical clocks and Cs primary frequency standards: $d/dt[\ln(\nu_{Hg^+}/\nu_{Cs})] = (0.37 \pm 0.39) \cdot 10^{-15}\,\mathrm{yr}^{-1}$ (data from figure 7(a)), $d/dt[\ln(\nu_H/\nu_{Cs})] = (1.2 \pm 4.4) \cdot 10^{-15}\mathrm{yr}^{-1}$ (data from [56]), $d/dt[\ln(\nu_{Yb+}/\nu_{Cs})] = (3.2 \pm 6.3) \cdot 10^{-15}\mathrm{yr}^{-1}$ (data from [55]). The contribution of the relativistic part for H is negligible ($N_H \approx 0$) and for Yb^+ is $N_{Yb} \approx 0.9$ [4].

Plotting the function

$$y = Nx - \frac{d}{dt}\ln\left(\frac{\nu_{Hg^+}}{\nu_{Cs}}\right),$$

(10)

where $x = \frac{\dot{\alpha}}{\alpha}$ and $y = \frac{d}{dt}\ln\left(\frac{\mu_{Cs}}{\mu_B}\right)$ and using the results reported above for Hg^+, H, and Yb^+ the figure 8 can be obtained.

The fractional uncertainty of the coupled variation can be estimated using a two-dimensional chi-square function, which provides the ellipse in the figure 8 for the 1σ statistical limit and projecting the ellipse on the x and y axis gives the following temporal constraints:

$$-1.5 \cdot 10^{-15} < \frac{\dot{\alpha}}{\alpha} < 0.4 \cdot 10^{-15}\,\mathrm{yr}^{-1}$$
$$-2.7 \cdot 10^{-15} < \frac{d}{dt}\ln\left(\frac{\mu_{Cs}}{\mu_B}\right) < 8.6 \cdot 10^{-15}\,\mathrm{yr}^{-1}.$$

(11)

The dependence of the HFS frequency on magnetic moments can be written in terms of other fundamental constants. In particular, using data from frequency comparison between two HFS transitions (Rb vs. Cs in [57]) and a model (e.g. the Schmidt model) which provides the dependence between the nuclear magnetic moment and the nuclear gyromagnetic factors, together
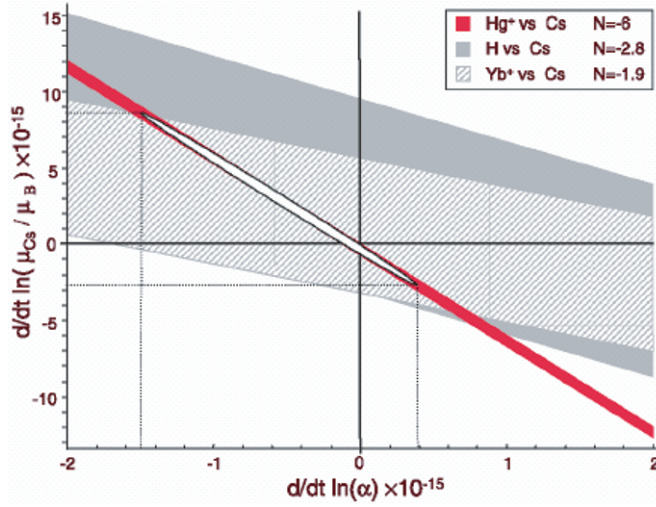
Fig. 8. Coupled constraint of $\dot{\alpha}/\alpha$ and $d/dt[\ln(\mu_{Cs}/\mu_B)]$. Projection of the white ellipse on the x and y axes provides the results reported in equation (11).

with the result for magnetic moments in equation (11), it is possible to extract an evaluation of the possible temporal dependence of the ratio m_e/M_p, where m_e is the mass of the electron and M_p is the mass of the proton. This evaluation is actually dependent on the nuclear model used, which cannot provide an accuracy consistent with the measurements. Recently, a different parametrization has been proposed in [58], where the magnetic moments have been written in terms of the parameters $X_e = (m_e/\Lambda_{QCD})$ and $X_q = (m_q/\Lambda_{QCD})$ where m_e is the mass of the electron, m_q is the mass of the quark and Λ_{QCD} is the quantum chromodinamic scale.

The measurement of the frequency ratio of Al^+ to Hg^+ provides a cleaner temporal constraint on $\dot{\alpha}/\alpha$ because it is a direct frequency ratio and does not involve the Cs metric and nuclear magnetic moments. The sensitivity on $\dot{\alpha}/\alpha$ given by the Al^+ to Hg^+ ratio is also high, owing to the large negative relativistic contribution for Hg^+ and the unprecedented accuracy of the measurement data. From equation (9), temporal variation of Al^+ to Hg^+ becomes:

$$\frac{\frac{d}{dt}\left(\frac{\nu_{Al+}}{\nu_{Hg+}}\right)}{\frac{\nu_{Al+}}{\nu_{Hg+}}} = \frac{\dot{\alpha}}{\alpha}N, \tag{12}$$

where $N = N_{Hg+} - N_{Al+} \approx -3.2$ and $N_{Al+} \approx 0$. For the evaluation of $\dot{\alpha}/\alpha$, measurements data reported in figure 7(b) were condensed in five points, spanning from December 2006 to December 2007.

The line connecting the two extreme points provides the following constraint [32]:

$$\frac{d}{dt}\ln\left(\frac{\nu_{Al+}}{\nu_{Hg+}}\right) = (-5.3 \pm 7.9) \cdot 10^{-17} \text{ yr}^{-1}, \tag{13}$$

which offers a ten-fold improvement to the best previous result. The intermediate points were excluded because the evaluation of their systematic uncertainties was incomplete. Estimation of α temporal variation reported in equation (13) can be used to upgrade the coupled constraint on $\dot{\alpha}/\alpha$ and $d/dt\ln(\mu_{Cs}/\mu_B)$ described before. As the Al^+/Hg^+ frequency ratio does not depend on $d/dt\ln(\mu_{Cs}/\mu_B)$, it is represented as a vertical band in figure 9(b). Projecting the white ellipse of figure 9(b) on the x and y axis the following updated estimation can be obtained:

$$\frac{\dot{\alpha}}{\alpha} = (-1.6 \pm 2.3) \cdot 10^{-17} \text{ yr}^{-1}$$
$$\frac{d}{dt}\ln\left(\frac{\mu_{Cs}}{\mu_B}\right) = (-1.9 \pm 4.0) \cdot 10^{-16} \text{ yr}^{-1}. \tag{14}$$
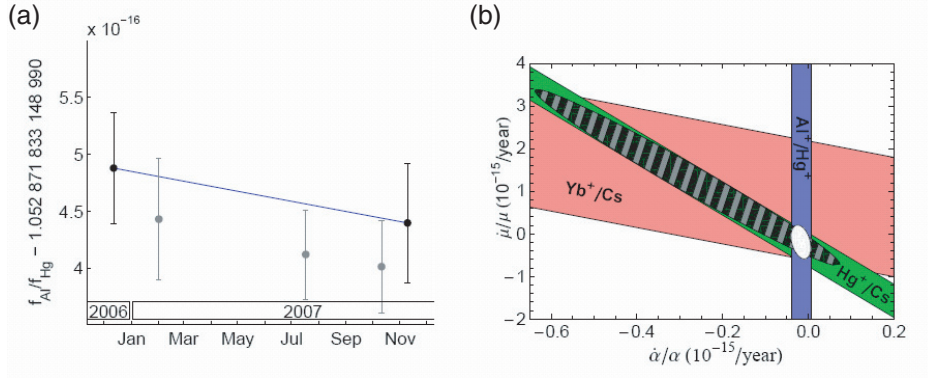
Fig. 9. (a) Temporal variation of α is estimated with the line connecting the two extreme points, which are separated by a duration of a year (b) Coupled constraint of $\dot{\alpha}/\alpha$ and $d/dt \ln(\mu_{Cs}/\mu_B)$. Projection of the the white ellipse on the x and y axes provides the results of equation (14) [32].

6.2 Local position invariance test

General relativity predicts that the frequency ν of an atomic clock depends on the gravitational potential according to the following equation, which describes the so called "gravitational redshift":

$$\frac{\Delta\nu}{\nu} = -\frac{\Delta U}{c^2},\tag{15}$$

where $\Delta\nu$ is the frequency change due to to the variation ΔU of the gravitational potential. Local Position Invariance (LPI) predicts that this change does not depend on the internal "details" of the clock structure. The allowance of a small and linearized breakdown of the LPI is described by the coefficient β in the following relation:

$$\frac{\Delta\nu}{\nu} = -(1+\beta)\frac{\Delta U}{c^2}.\tag{16}$$

If the frequency ratio between two atomic clocks is measured in a varying gravitational potential equation (16) gives

$$\frac{\Delta(\nu_1/\nu_2)}{(\nu_1/\nu_2)} = (\beta_2 - \beta_1)\frac{\Delta U}{c^2}.\tag{17}$$

The gravitational potential on the earth surface changes annually due to the elliptical orbit of the earth around the sun. Hence a frequency comparison between two different atomic clocks spanning more than one year can offer a limit to any possible LPI violation [59,60]. The gravitational potential change due to the earth's orbit around the sun is

$$\frac{\Delta U}{c^2} \approx -2\frac{(GMe\cos\phi)}{ac^2},\tag{18}$$

where G is the gravitational constant, M is the solar mass, e is the orbit eccentricity, c is the speed of light, ϕ is the phase of the annual change, which is zero at the perihelion. The annual peak to peak variation in the gravitational potential is given by

$$\frac{\Delta U_{max}}{c^2} = 3.3 \cdot 10^{-10},\tag{19}$$

and the value contains both the solar leading term of equation 18 and the contributions of minor celestial bodies. If LPI is violated then $|\beta_2 - \beta_1|$ and the clock ratio data will be correlated with the seasonal variation of ΔU. Then fitting the Hg^+ to Cs ratio data reported in figure 7(b) with

a cosine function, whose phase can be either the same or the opposite as ϕ in equation (17), the following estimation is obtained:

$$|\beta_{Hg} - \beta_{Cs}| = (2 \pm 3.5) \cdot 10^{-6}. \tag{20}$$

A different LPI test [61], performed with a comparison between Cs and H HFS structure transition which uses data from Primary frequency standards and H masers which spans several years provided the following result:

$$|\beta_H - \beta_{Cs}| = (0.1 \pm 1.6) \cdot 10^{-6}. \tag{21}$$

The relevance of the two LPI tests cannot be directly compared, because the sensitivity of β_{Hg} and β_H with respect to the variation of the gravitational potential could be different. In a recent paper [62], Flambaum has proposed to test the gravitation potential sensitivity of the fundamental constants involved in the atomic transitions.

References

1. V.V. Flambaum, Int. J. Mod. Phys. A **22**, 4937 (2007)
2. S. Lea, Rep. Prog. Phys. **70**, 1773 (1995)
3. T. Damour, F. Dyson, Nucl. Phys. B **480**, 37 (1996)
4. V.A. Dzuba, V.V. Flambaum, J.K. Webb, Phys. Rev. A **59**, 230 (1999)
5. M.T. Murphy, J. Webb, V. Flambaum, Mon. Not. R. Astron. Soc. **345** (2003)
6. S.A. Levshakov, M. Centurion, P. Molaro, S. D'Odorico, Astron. Astrophys. **434**, 827 (2005)
7. W.H. Oskay, W.M. Itano, J.C. Bergquist, Phys. Rev. Lett. **94**, 163001 (2006)
8. T. Rosenband, P.O. Schmidt, D.B. Hume, W.M. Itano, T.M. Fortier, J.E. Stalnaker, K. Kim, S.A. Diddams, J.C.J. Koelemeij, J.C. Bergquist, et al., Phys. Rev. Lett. **98**, 220801 (2007)
9. G. Wilpers, C. Oates, S. Diddams, A. Bartels, T. Fortier, W. Oskay, J. Bergquist, S. Jefferts, T. Heavner, T. Parker, et al., Metrologia **44**, 146 (2007)
10. Z. Barber, C. Hoyt, C. Oates, L. Hollberg, A. Taichenachev, V. Yudin, Phys. Rev. Lett. **96**, 083002 (2006)
11. A.D. Ludlow, T. Zelevinsky, G.K. Campbell, S. Blatt, M.M. Boyd, M.H.G. de Miranda, M.J. Martin, J.W. Thomsen, S.M. Foreman, J. Ye, et al., Science **319**, 1805 (2008)
12. S.R. Jefferts, J.H. Shirley, T.E. Parker, T.P. Heavner, D.M. Meekhof, C.W. Nelson, F. Levi, G. Costanzo, A. DeMarchi, R.E. Drullinger, et al., Metrologia **39**, 321 (2002)
13. P.L. Bender, J.L. Hall, R.H. Garstang, F.M.J. Pichanick, W.W. Smith, R.L. Barger, J.B. West, Bull. Am. Phys. Soc. **21**, 599 (1976)
14. J.C. Bergquist, D.J. Wineland, W.M. Itano, H. Hemmati, H.U. Daniel, G. Leuchs, Phys. Rev. Lett. **55**, 1567 (1985)
15. H. Dehmelt, IEEE Trans. Instrum. Meas. **IM-31**, 83 (1982)
16. J.C. Bergquist, R.G. Hulet, W.M. Itano, D.J. Wineland, Phys. Rev. Lett. **57**, 1699 (1986)
17. C. Salomon, D. Hils, J.L. Hall, J. Opt. Soc. Am. B **5**, 1576 (1988)
18. B.C. Young, F.C. Cruz, J.C. Bergquist, W.M. Itano, Phys. Rev. Lett. **82**, 3799 (1999)
19. R. Holzwarth, T. Udem, T. Haensch, J. Knight, W. Wadsworth, P. Russell, Phys. Rev. Lett. **85**, 2264 (2000)
20. D. Jones, S. Diddams, J. Ranka, A. Stentz, R. Windeler, J. Hall, S. Cundiff, Science **288**, 635 (2000)
21. S.A. Diddams, T. Udem, J.C. Bergquist, E.A. Curtis, R.E. Drullinger, L. Hollberg, W.M. Itano, W.D. Lee, C.W. Oates, K.R. Vogel, et al., Science **293**, 825 (2001)
22. M.E. Poitzsch, J.C. Bergquist, W.M. Itano, D.J. Wineland, Rev. Sci. Instrum. **67**, 129 (1996)
23. D.J. Berkeland, F.C. Cruz, J.C. Bergquist, Appl. Opt. **36**, 4159 (1997)
24. D.J. Berkeland, M.G. Boshier, Phys. Rev. A **65**, 033413 (2002)
25. D.J. Berkeland, M.G. Boshier (2006) (private communication)

26. W.M. Itano, J.C. Bergquist, A. Brusch, S.A. Diddams, T.M. Fortier, T.P. Heavner, L. Hollberg, D.B. Hume, S.R. Jefferts, L. Lorini, et al., *Proc. 2007 SPIE Conf.* (2007), Vol. 6673, p. 667303
27. T.W. Haensch, B. Couillaud, Opt. Commun. **35**, 441 (1980)
28. R.W.P. Drever, J.L. Hall, et al., Appl. Phys. B **31**, 97 (1983)
29. D.H. Crandall, R.A. Phaneuf, G.H. Dunn, Phys. Rev. A **11**, 1223 (1975)
30. W.H. Oskay, S.A. Diddams, E.A. Donley, T. Fortier, T.P. Heavner, L. Hollberg, W.M. Itano, S.R. Jefferts, M.J. Jensen, K. Kim, et al., Phys. Rev. Lett. **97**, 020801 (2006)
31. D.J. Berkeland, J.D. Miller, J.C. Bergquist, W.M. Itano, D.J. Wineland, J. Appl. Phys. **83**, 5025 (1998)
32. T. Rosenband, D.B. Hume, P.O. Schmidt, C.W. Chou, A. Brusch, L. Lorini, W.H. Oskay, R.E. Drullinger, T.M. Fortier, J.E. Stalnaker, et al., Science **319**, 1808 (2008)
33. W. Itano, J. Res. Natl. Instrum. Stan. **105**, 829 (2001)
34. M. Barrett, B.L. DeMarco, T. Schaetz, D. Leibfried, J. Britton, J. Chiaverini, W.M. Itano, B.M. Jelenkovic, J.D. Jost, C. Langer, et al., Phys. Rev. A. **68**, 042302 (2003)
35. D. Wineland, J. Bergquist, J. Bollinger, R. Drullinger, W. Itano, *Proc. 2001 Freq. Stand. Metrology Symp.* (2001), pp. 361–368
36. P.O. Schmidt, T. Rosenband, C. Langer, W.M. Itano, J.C. Bergquist, D.J. Wineland, Science **309**, 749 (2005)
37. D. Hume, T. Rosenband, D.J. Wineland, Phys. Rev. Lett. **99**, 120502 (2007)
38. T. Rosenband, W.M. Itano, P. Schmidt, D. Hume, J. Koelemeij, J.C. Bergquist, D.J. Wineland, *Proc. 2006 EFTF Conf.* (2006), pp. 289–292
39. T.P. Heavner, S.R. Jefferts, E.A. Donley, J.H. Shirley, T. Parker, Metrologia **42**, 411 (2005)
40. T. Parker, S. Jefferts, T. Heavner, E. Donley, Metrologia **42**, 423 (2005)
41. T. Fortier, A. Bartels, S. Diddams, Opt. Lett. **31**, 1011 (2006)
42. B.R. Washburn, R.W. Fox, N.R. Newbury, J.W. Nicholson, K. Feder, P. Westbrook, Opt. Express **12**, 4999 (2004)
43. J. Bergquist, W. Itano, D. Wineland, *Proc. 1992 Intl. School Phys. E. Fermi* (1992), pp. 359–376
44. T. Udem, S.A. Diddams, K.R. Vogel, C.W. Oates, E.A. Curtis, W.D. Lee, W.M. Itano, R.E. Drullinger, J.C. Bergquist, L. Hollberg, Phys. Rev. Lett. **86**, 4996 (2000)
45. T.M. Ramond, S.A. Diddams, L. Hollberg, A. Bartels, Opt. Lett. **27**, 1842 (2002)
46. D. Yu, M. Weiss, T. Parker, Metrologia **44**, 91 (2007)
47. U. Tanaka, J. Bergquist, S. Bize, S. Diddams, R. Drullinger, L. Hollberg, W. Itano, C. Tanner, D. Wineland, IEEE T. Instrum. Meas. **52**, 245 (2003)
48. S. Bize, S.A. Diddams, U. Tanaka, C.E. Tanner, W.H. Oskay, R.E. Drullinger, T.E. Parker, T.P. Heavner, S.R. Jefferts, L. Hollberg, et al., Phys. Rev. Lett. **90**, 150802 (2003)
49. J. Stalnaker, S.A. Diddams, T. Fortier, K. Kim, L. Hollberg, J.C. Bergquist, W.M. Itano, M.J. Delaney, L. Lorini, W.H. Oskay, et al., Appl. Phys. B. **89**, 167 (2007)
50. I. Coddington, W.C. Swann, L. Lorini, J.C. Bergquist, Y.L. Coq, C.W. Oates, Q. Quraishi, K.S. Feder, J.W. Nicholson, P.S. Westbrook, et al., Nature Photonics **1**, 283 (2007)
51. S.G. Karshenboim, Can. J. Phys. **78**, 639 (2000)
52. T. Fortier, N. Ashby, J.C. Bergquist, M.J. Delaney, S.A. Diddams, T.P. Heavner, L. Hollberg, W.M. Itano, S.R. Jefferts, K. Kim, et al., Phys. Rev. Lett. **98**, 070801 (2007)
53. E. Peik, B. Lipphardt, H. Schnatz, C. Tamm, S. Weyers, R. Wynands, *Proceedings of the 11th Marcel Grossmann Meeting, Berlin* (2006)
54. E.J. Angstmann, V.A. Dzuba, V.V. Flambaum, Phys. Rev. A **70**, 014102 (2004)
55. E. Peik, et al., Phys. Rev. Lett. **93**, 170801 (2004)
56. M. Fischer, et al., Phys. Rev. Lett. **92**, 230802 (2004)
57. H. Marion, F.P.D. Santos, M. Abgrall, S. Zhang, Y. Sortais, S. Bize, I. Maksimovic, D. Calonico, J. Gruenert, C. Mandache, et al., Phys. Rev. Lett. **90**, 150801 (2003)
58. V.V. Flambaum, A. Tedesco, Phys. Rev. C **73**, 055501 (2006)
59. A. Godone, C. Novero, P. Tavella, Phys. Rev. D **51**, 319 (1995)
60. A. Bauch, S. Weyers, Phys. Rev. D **65**, 081101 (2001)
61. N. Ashby, T.P. Heavner, S.R. Jefferts, T.E. Parker, A.G. Radnaev, Y.O. Dudin, Phys. Rev. Lett. **98**, 070802 (2007)
62. V.V. Flambaum, E.V. Shuryak (2007) [`arXiv:physics/0701220`]